Development of Monolithic Michelson Interferometer for RV Measurement in IR

Ji Wang[a], Xiaoke Wan[a] and Jian Ge[a]

[a]Department of Astronomy, University of Florida, USA

ABSTRACT

We present a fixed delay interferometer to be installed in IR-ET (Infra-Red Exoplanets Tracker). We introduce the design, fabrication and testing processes. In particular, we present a new methodology of computing the fundamental limit of radial velocity (RV) measurement given by photon noise for DFDI (Dispersed Fixed Delay Interferometer) method as opposed to conventional echelle method. The new method is later used to determine the optical path difference (OPD) of the IR-ET interferometer. In addition, we introduce a novel method of monitoring the stability of the interferometer for IR-ET in broad-band using fourier-transform white-light scanning interferometry technique. The new method can be potentially expanded and applied to thermo-optic effect measurement if temperature control system is introduced into the experiment. The thermal response of the optical system is 3500 $m/s/^{\circ}C$. We find that the RV calibration precision of 'Bracketing' method is 1.74 m/s without temperature control.

Keywords: Infrared, Interferometer, Radial Velocity, Fourier Optics

1. INTRODUCTION

Radial velocity (RV) technique is widely used in exoplanets searching instruments and has led to great success, most of the exoplanets detected as of today are discovered by RV technique*. Reaching better than 1 m/s RV precision is achieved routinely for bright and stable stars.[1] In most of cases the RV precision is limited by photon noise. The previous studies of photon noise impact on RV precision can be found in Ref 2 and 3. However, the previous studies considered RV precision given photon noise for conventional echelle method, in which the centroid shift of stellar absorption lines is measured to extract RV. Ge et al. (2002) and Erskine et al. (2003) introduced a new method of conducting precise RV measurement, namely, DFDI (Dispersed Fixed Delay Interferometer),[4] also known as Externally Dispersed Interferometry method,[5] in which RV is measured by monitoring stellar fringe phase shift. DFDI method is able to achieve the same RV precision with lower spectral resolution, which effectively enhances the throughput of the instrument.

Fixed delay interferometer plays an crucial role as a fine spectral resolution elements for high precision RV measurement.[4-6] Doppler velocity shift measured in DFDI method can be expressed as $\Delta v = \frac{c}{\nu}\Delta\phi/\frac{d\phi}{d\nu}$ with c the speed of light, ν the optical frequency and $\frac{1}{2\pi}\frac{d\phi}{d\nu}$ the group delay of the interferometer. The group delay is often referred as optical path difference (OPD) in general occasions because OPD of an achromatic interferometer equals $\frac{c}{2\pi}\frac{d\phi}{d\nu}$. Artificial RV signal is produced due to thermal response of group delay for the interferometer. However, temporally slow change in OPD of interferometer can be calibrated using 'Bracketing' method, in which spectra of wavelength calibration sources are taken before and after exposure of science target. In order to achieve high RV precision (i.e. low RV uncertainty), interferometer has to be temperature controlled to ensure a fixed group delay. In laboratory experiment, we use a frequency-stabilized laser as a frequency reference to track subtle drift in optical path difference. However, an frequency-stabilized laser source in infrared (IR) is not as common and economically prohibitive. Therefore, we develop a novel method of monitoring the stability of interferometer in IR using fourier-transform white-light scanning interferometry. Not only does it expand the measurable frequency region but also it is capable of monitoring stability in broad-band within frequency region of interest. This method can also be potentially used in thermo-optic effect measurement in broad-band. In comparison, the previous measurements are conducted in laser frequencies.[7,8]

Further author information: (Send correspondence to Ji Wang)
Ji Wang: E-mail: jwang@astro.ufl.edu, Telephone: 1 352 392 2052(281)
*http://exoplanet.eu/; http://exoplanets.org/

We present the methodology of computing the fundamental limit of RV measurement in §2. The Design of the IR-ET interferometer is introduced in §3. We focus on the thermal stability of the interferometer and present a new method of monitoring thermal stability in §4. We discuss the precision of RV calibration using the 'Bracketing' method in §5. Discussion and conclusion are given in §6.

2. FUNDAMENTAL LIMIT OF RADIAL VELOCITY MEASUREMENT

2.1 Radial Velocity Uncertainty Using Conventional Echelle Method

Following the method described in Ref. 3, let $S_0(\nu)$ designate an intrinsic stellar spectrum. We also consider A_0, a digitalized and calibrated spectrum as a noise-free template spectrum for differential RV measurement. A_0 is related to $S_0(\nu)$ via the following equation:

$$A_0(i) = S_0(\nu) \otimes PSF(\nu), \tag{1}$$

where $PSF(\nu)$ is spectral response function. Another spectrum A is taken at a different time with a tiny doppler shift, which is small relative to the typical line width of an intrinsic stellar absorption. We assume the two spectra have the same continuum level. The doppler shift is given by:

$$\frac{\delta v}{c} = \frac{\delta \nu}{\nu}, \tag{2}$$

where c is speed of light and ν is optical frequency. The observable intensity change at a given pixel i can be expressed:

$$A(i) - A_0(i) = \frac{\partial A_0(i)}{\partial \nu(i)} \delta \nu(i) = \frac{\partial A_0(i)}{\partial \nu(i)} \cdot \frac{\delta v(i)}{c} \cdot \nu(i). \tag{3}$$

The doppler shift is then given by rearranging equation (3):

$$\frac{\delta v(i)}{c} = \frac{A(i) - A_0(i)}{\frac{\partial A_0(i)}{\partial \nu(i)} \cdot \nu(i)}. \tag{4}$$

Spectrum A_0 is considered as noise-free and the noise of spectrum A is the quadratic sum of photon noise and detector noise σ_D:

$$A(i)_{rms} = \sqrt{A(i) + \sigma_D^2}. \tag{5}$$

Equation (5) is approximated under photon-noise limit condition as $A(i)_{rms} = \sqrt{A(i)}$. Therefore, the RV uncertainty at pixel i is given by:

$$\frac{\delta v(i)_{rms}}{c} = \frac{\sqrt{A(i)}}{\frac{\partial A_0(i)}{\partial \nu(i)} \cdot \nu(i)}. \tag{6}$$

In order to maximize the doppler sensitivity and minimize the noise, the entire spectral range has to be used. The overall RV uncertainty for entire spectral range is given by:

$$\frac{\delta v_{rms}}{c} = \sqrt{\frac{1}{\sum_i \left(\frac{\delta v(i)_{rms}}{c} \right)^{-2}}} = \frac{1}{\sqrt{\sum_i \left[\left(\frac{\partial A_0(i)}{\partial \nu(i)} \right)^2 \nu(i)^2 / A(i) \right]}} \equiv \frac{1}{\sqrt{\sum_i W(i)}} \equiv \frac{1}{Q \sqrt{\sum_i A_0(i)}}. \tag{7}$$

In Ref. 3, Q is defined as:

$$Q \equiv \frac{\sqrt{\sum_i W(i)}}{\sqrt{\sum_i A_0(i)}}. \tag{8}$$

Q factor is independent of flux and represents the doppler information given intrinsic stellar spectrum and instrument spectral resolution. According to Equation (7), we can calculate RV uncertainty under photon-noise limit condition given Q factor and photon flux $\sum_i A_0(i)$ within spectral range.

2.2 Radial Velocity Uncertainty Using Dispersed Fixed Delay Interferometer Method

Dispersed Fixed Delay Interferometer (DFDI) method is explained in detail in Ref. 4 and 5. DFDI method is performed by coupling an interferometer with a post disperser. Doppler shift of stellar absorption line is measured by monitoring the phase shift of fringe instead of measuring the centroid shift of stellar absorption line as in conventional echelle method. The resulting fringing spectrum is recorded on a 2-D detector.

Let $S_0(\nu)$ designate intrinsic stellar spectrum. After propagating through an interferometer, the 2-D flux distribution is given by:

$$F_0(\nu, y) = \gamma(\nu) \cdot S_0(\nu, y) \cdot [1 + \cos(\phi(\nu, y))], \tag{9}$$

where γ is visibility and ϕ is given by:

$$\phi(\nu, y) = \frac{2\pi\nu\tau(y)}{c}, \tag{10}$$

where y is the coordinate in the direction perpendicular to dispersion direction (i.e. slit direction), and τ is OPD of the interferometer and it is designed to be tilted along slit direction such that we obtain multiple fringes in each frequency channel. F_0 is then convolved with spectral response function $PSF(\nu)$ to obtain a 2-D digitalized flux distribution on detector:

$$B_0(i, j) = F_0(\nu, y) \otimes PSF(\nu), \tag{11}$$

where i is the pixel number along dispersion direction, j is the pixel number along slit direction. Note that the doppler shift is measured along slit direction by monitoring the intensity change at given pixel in DFDI. The observable intensity change at given pixel (i, j) in DFDI is expressed by:

$$B(i, j) - B_0(i, j) = \frac{\partial B_0(i, j)}{\partial \nu(i)} \delta\nu(i) = \frac{\partial B_0(i, j)}{\partial \nu(i)} \cdot \frac{\delta v(i, j)}{c} \cdot \nu(i), \tag{12}$$

where B_0 is noise-free template frame and B is a frame taken at a different time with a tiny doppler shift. The doppler shift is calculated by monitoring the intensity change at given pixel in the equation:

$$\frac{\delta v(i, j)}{c} = \frac{B(i, j) - B_0(i, j)}{\frac{\partial B_0(i, j)}{\partial \nu(i)} \cdot \nu(i)}. \tag{13}$$

Frame B_0 is considered as noise-free and the noise of frame B is the quadratic sum of photon noise and detector noise σ_D:

$$B(i, j)_{rms} = \sqrt{B(i, j) + \sigma_D^2}. \tag{14}$$

Equation (14) is approximated under photon-noise limit condition as $B(i, j)_{rms} = \sqrt{B(i, j)}$. Therefore, the RV uncertainty at pixel (i, j) is given by:

$$\frac{\delta v(i,j)_{rms}}{c} = \frac{\sqrt{B(i,j)}}{\frac{\partial B_0(i,j)}{\partial \nu(i)} \cdot \nu(i)}. \tag{15}$$

The RV uncertainty for ith frequency channel is given by:

$$\frac{\delta v(i)_{rms}}{c} = \sqrt{\frac{1}{\sum_j \left(\frac{\delta v(i,j)_{rms}}{c}\right)^{-2}}} = \sqrt{\frac{1}{\sum_j \left[\left(\frac{\partial B_0(i,j)}{\partial \nu(i)}\right)^2 \nu(i)^2 / B(i,j)\right]}}. \tag{16}$$

The overall RV uncertainty for entire spectral range is given by:

$$\frac{\delta v_{rms}}{c} = \sqrt{\frac{1}{\sum_i \left(\frac{\delta v(i)_{rms}}{c}\right)^{-2}}} = \sqrt{\frac{1}{\sum_{i,j} \left(\frac{\delta v(i,j)_{rms}}{c}\right)^{-2}}} \equiv \frac{1}{\sqrt{\sum_{i,j} W(i,j)}} \equiv \frac{1}{Q \sqrt{\sum_{i,j} B_0(i,j)}}, \tag{17}$$

where

$$W(i,j) = \left(\frac{\partial B_0(i,j)}{\partial \nu(i)}\right)^2 \nu(i)^2 / B(i,j), \tag{18}$$

and

$$Q \equiv \frac{\sqrt{\sum_{i,j} W(i,j)}}{\sqrt{\sum_{i,j} B_0(i,j)}}. \tag{19}$$

Equation (19) calculates the Q factor for DFDI method, which is also independent of flux and represents the doppler information that can be extracted by DFDI method. According to Equation (17), we can calculate RV uncertainty under photon-noise limit condition given Q factor and photon flux $\sum_{i,j} B_0(i,j)$ within spectral range.

3. INTERFEROMETER DESIGN

3.1 Delay Selection

In DFDI method, high doppler sensitivity is achieved by optimizing the OPD of the interferometer. We choose the OPD of interferometer that maximize the Q factor. IR-ET is designed to conduct exoplanet search around mid-late M type stars, whose effective temperature T_{eff} range is from 2000K to 3500K. The wavelength coverage of IR-ET is from $8000\mathring{A}$ to $13500\mathring{A}$ and spectral resolution is 22000. We use high resolution synthetic stellar spectra generated by PHOENIX code[9, 10] because observed spectra of low mass stars do not have sufficient resolution and T_{eff} coverage for our simulations. Reiners et al. (2010) have conducted several comparisons between PHOENIX model spectra and observed spectra and conclude that the model spectra are accurate enough for simulations.[11]

Fig. 1 shows RV uncertainties calculated for a variety of T_{eff} and $Vsini$ as a function of OPD. We consider rotational broadening effect in our simulation. Note that rotational broadening effect decreases Q factor, resulting in lower doppler sensitivity. IR-ET is designed to focus on slow rotators (stars with small $Vsini$, i.e. $Vsini \leq 10km$). Jenkins et al. (2009) compile $Vsini$ of M type stars available from literatures from which we generate Fig. 2.[12] Statistically, 80% of M type stars have rotation velocity $Vsini$ less than 10 km/s and 50% have $Vsini$ around 2 km/s. According to our simulation, we decide to choose the OPD of interferometer to be 18 mm.
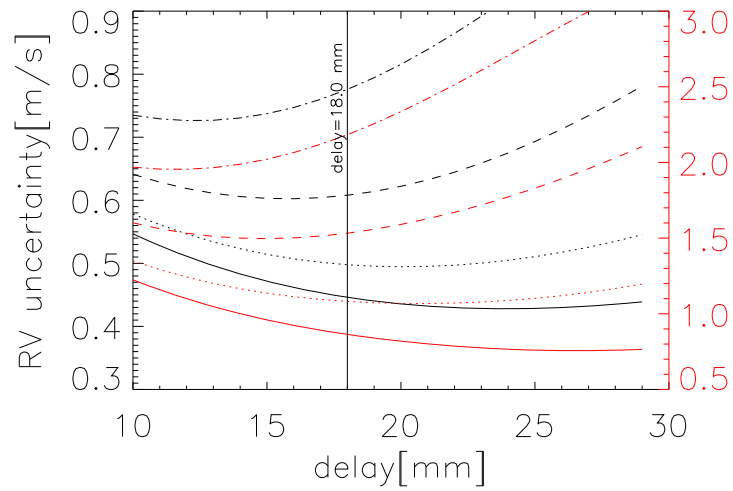
Figure 1. RV uncertainties as a function of OPD for a variety of T_{eff} (black-2000K; red-2800K) and $V\,sini$ (dashed-dotted: 7 km/s; dashed: 5 km/s; dotted: 3 km/s; solid: 1 km/s).
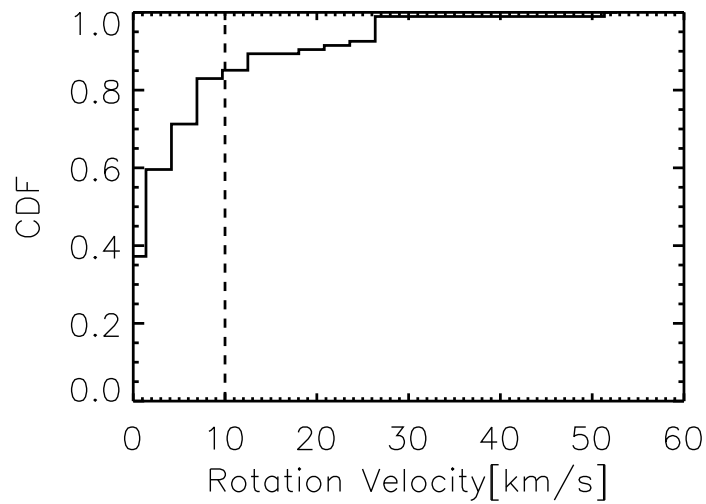

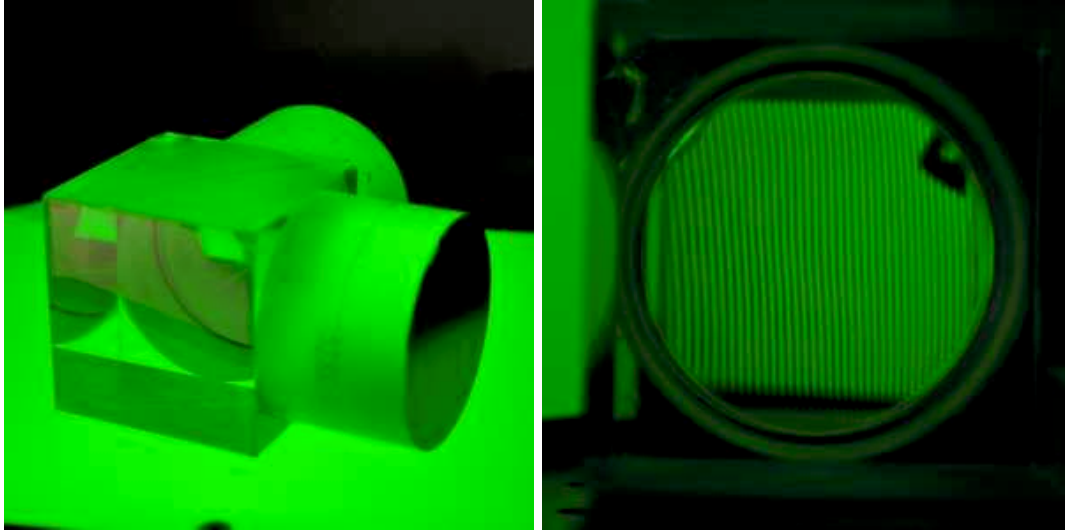Figure 2. Cumulative distribution function of $V\,sini$, dashed line represent $V\,sini = 10\ km/s$

Figure 3. Pictures of IR-ET interferometer. The fringe density is 1.06 mm/fringe at $5410\mathring{A}$

3.2 Field Compensation

The OPD of the IR-ET interferometer is 18.0 mm, which optimizes doppler sensitivity of the instrument given the stellar spectrum features of science targets. The interferometer consists of three parts, a 2-inch BK7 beam splitter, a BK7 second surface mirror and a LAK7 second surface mirror. It is designed to be field-compensated (Equation (20)) so that it provides high visibility fringes over a wide field of view which is beneficial for doppler velocity measurement.

$$D_1/n_1 = D_2/n_2 \tag{20}$$

where D and n are mirror thickness and refractive index and subscript 1 and 2 denote BK7 and LAK7 respectively. OPD τ_0 is determined by equation (21):

$$\tau_0 = 2 \cdot (D_2 n_2 - D_1 n_1) \tag{21}$$

Solving equation (20) and (21) with $\tau_0 = 18\ mm$, $n_1 = 1.5067$ and $n_2 = 1.6383$ at $\lambda_0 = 1060\ nm$, we obtain $D_1 = 32.77\ mm$ and $D_2 = 35.63\ mm$. Fig. 3 are pictures of IR-ET under the illumination of Hg lamp.

4. INTERFEROMETER THERMAL STABILITY

Conventionally, we use frequency-stabilized He-Ne laser ($\lambda_0 = 0.6328\mu m$) to monitor the phase drift at a fixed position of interferometer in order to track the stability of the interferometer. However, the conventional method is no longer applicable for the following reasons: 1) an frequency-stabilized laser source in IR is not as common as in visible band and economically prohibitive; 2) Interferometer stability in IR cannot be simply scaled from visible band because of dispersion of glass. Therefore, we develop a new method of monitoring the stability of interferometer in IR using fourier-transform white-light scanning interferometry technique. Not only does it expand the measurable frequency region but also it is capable of monitoring stability at multiple frequencies within frequency region of interest.

4.1 Theory

We incorporate the IR-ET interferometer into a Fourier Transform Spectrograph (FTS). As the scanning arm of FTS moves an adequate distance, we will see signal described in the following equation:

$$
\begin{aligned}
I(\nu) &= \int_{\nu} \bar{I} \cdot s(\nu) \cdot \left[1 + cos(\phi(\nu)) \right] \cdot \left[1 + cos(\phi_0(\nu)) \right] d\nu \\
&= \int_{\nu} \bar{I} \cdot s(\nu) \cdot \left[1 + cos(\phi_0(\nu)) + cos(\phi(\nu)) + (1/2) \cdot cos(\phi(\nu) + \phi_0(\nu)) + (1/2) \cdot cos(\phi(\nu) - \phi_0(\nu)) \right] d\nu, \\
&= C_s + W + W_+ + W_-
\end{aligned} \tag{22}
$$

where ϕ and ϕ_0 are the phase delay of scanning interferometer and IR-ET interferometer respectively, they are expressed as:

$$
\phi = \frac{2\pi\nu\tau}{c} = \frac{4\pi\nu}{c} \cdot \left[D(T) \cdot n_1(\nu, T) - \delta \right], \tag{23}
$$

$$
\phi_0 = \frac{2\pi\nu\tau_0}{c} = \frac{4\pi\nu}{c} \cdot \left[D_2(T_0) \cdot n_2(\nu, T_0) - D_1(T_0) \cdot n_1(\nu, T_0) \right], \tag{24}
$$

where τ is OPD, D is thickness of BK7 compensating plate in the fixed arm of scanning interferometer, δ is thickness of air in the scanning arm and subscript 0 denotes IR-ET interferometer. Equation (22) is composed of the following items:

$$
C_s = \int_{\nu} \bar{I} \cdot s(\nu) d\nu, \tag{25}
$$

$$
\int_{\nu} \bar{I} \cdot s(\nu) \cdot cos(\phi_0(\nu)) d\nu = 0, \tag{26}
$$

$$
W = \int_{\nu} \bar{I} \cdot s(\nu) \cdot cos(\phi(\nu)) d\nu, \tag{27}
$$

$$
W_+ = \frac{1}{2} \int_{\nu} \bar{I} \cdot s(\nu) \cdot cos(\phi(\nu) + \phi_0(\nu)) d\nu, \tag{28}
$$

$$
W_- = \frac{1}{2} \int_{\nu} \bar{I} \cdot s(\nu) \cdot cos(\phi(\nu) - \phi_0(\nu)) d\nu, \tag{29}
$$

The phase delay information is included in autocorrelation interferogram (Equation (27)) and cross correlation interferogram (Equation (28) and 29). Equation (26) equals to 0 because OPD of IR-ET interferometer is much larger than the coherence length of white light source, which is also the reason why we can separate peaks of W, W_+ and W_- in data analysis. Note that only within a small range of OPD scanning can we see signals because of wide band width of white light source. For example, the fourier phase φ we measured in interferogram W_- is given by:

$$
\varphi(\nu, T, T_0) = \phi(\nu) - \phi_0(\nu) = \frac{2\pi\nu}{c} \cdot \left[\tau(\nu, T) - \tau_0(\nu, T_0) \right]. \tag{30}
$$

A series of fourier phase φ_k and temperature $T_{0,k}$, $T_{0,k}$ are obtained after continuous monitoring, where k denotes data number. Changes in φ_k indicate optical system instability. Comparing series of fourier phase φ_k is meaningful only if it is measured at exactly the same δ, which is the air thickness in the scanning arm.
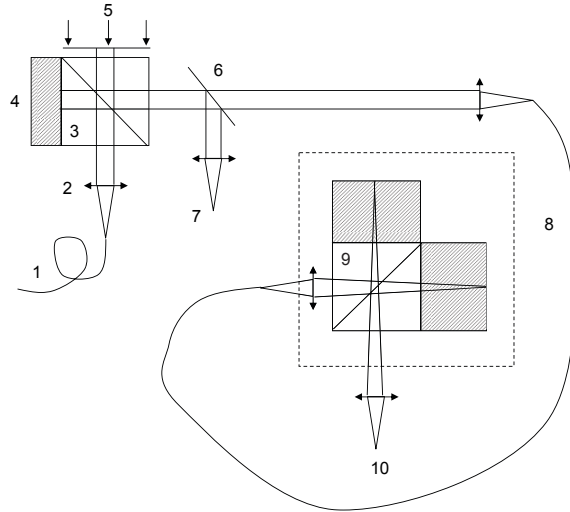
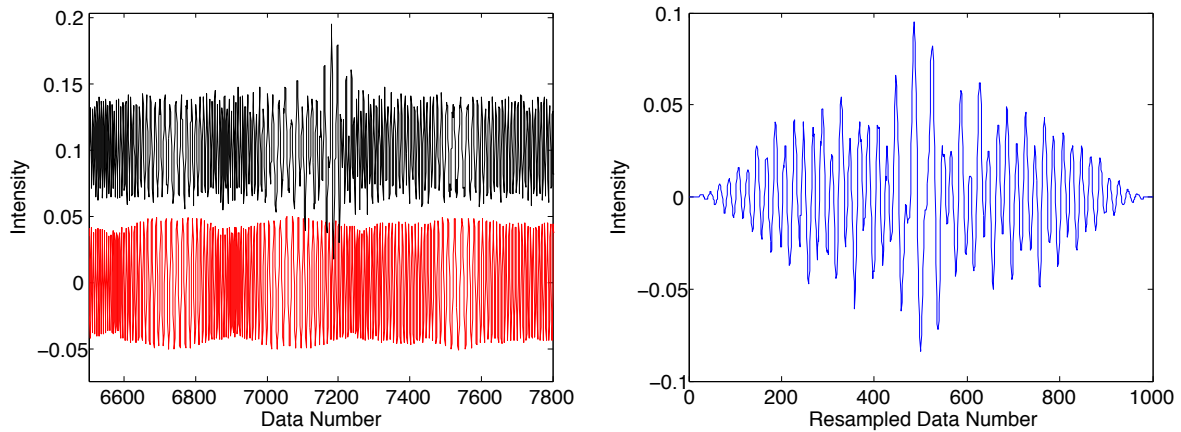Figure 4. Configuration of experiment

Figure 5. Left: Two channels of scanning data (black: white light signal, red: reference signal); right: Resampled and windowed data.

4.2 Experiment Design

Figure 4 is a configuration of experiment. white-light source and stabilized He-Ne laser ($\lambda_0 = 632.8nm$) are coupled into fiber 1 with 50 μm core diameter. Light from fiber 1 is fed to a scanning interferometer consisting of a 2-inch BK7 beam splitter 3, a BK7 second surface mirror 4 and a front surface mirror 5 mounted on a motor-driven linear stage. The thickness of second surface mirror 4 is chosen such that the scanning interferometer is field compensated at OPD of IR interferometer. A piece of glass plate 6 reflect at 45° angle the output light from scanning interferometer. A optical photodiode measures the reflecting power at 7, most of which is from stabilized He-Ne gas laser. The light going through the glass plate is fed into fiber 8, which directs the light to the IR interferometer 9. The output signal is measured at detector 10.

4.3 Data Analysis

Fig. 5 (Left) shows scanning time sequenced data. There are two channels of time sequenced data, reference signal $R\{i = 0, ..., N\}$ at detector 7 and white light signal $W\{i = 0, ..., N\}$ at detector 10. $R\{i = 0, ..., N\} = cos(2\pi\tau\{i = 0, ..., N\}\nu_r/c)$ is created by interference of red laser by the scanning interferometer. Due to variation of scanning speed, OPD of scanning interferometer τ does not uniformly change with time. In order to obtain
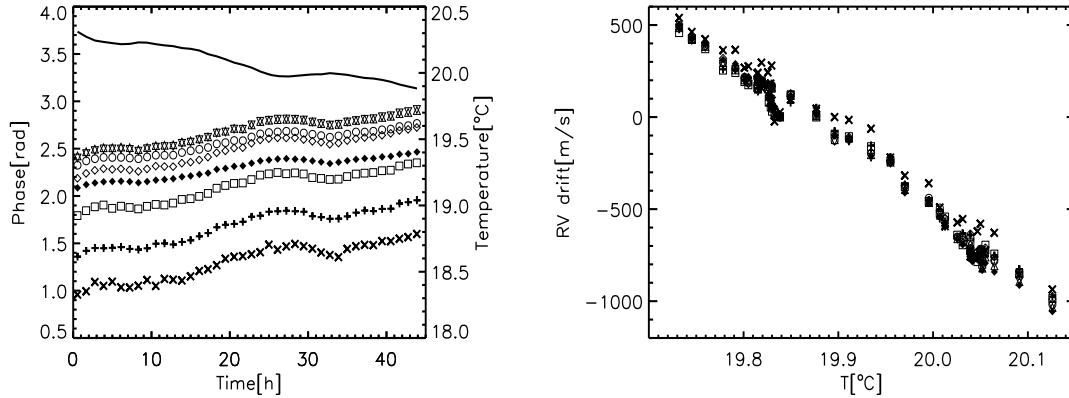
Figure 6. The left panel shows the fourier phase at different wavelength channel as a function of time over 44 hour continuous monitoring. The right panel shows the correlation between RV drift and room temperature. Different symbols represent different wavelength channels.

a uniformly sampled data, the time sequenced data is resampled in the space of phase shift of red laser. Time sequenced phase shift $\phi^R\{i = 0, ..., N\}$ can be obtained following a standard procedure.[13, 14] The analytic signal $H\{i = 0, ..., N\}$ of the reference signal is obtained by removing the negative frequency components of $R\{i = 0, ..., N\}$ in the fourier space followed by an inverse Fourier transform. The phase shift of red laser ϕ^R is obtained by calculating $Arg[Im(H_i)/Re(H_i)]$ and then unwrapping to eliminate 2π ambiguity. The average phase error is 0.01 rad which is determined by the S/N of the reference signal. Then we obtain the resampled white light signal $W\{j = 0, ..., M\}$ with step of $\Delta\phi_j^R = \pi/5$ which matches the actual sampling step such that $M \approx N$ (Fig. 5 right).

As stated in §4.1, we have to ensure that the fourier phase φ is measured at exactly the same δ, which is the air thickness in the scanning arm. According to equation (23), the same δ corresponds to the same ϕ^R if temperature effect on scanning interferometer is negligible. In fact, temperature changes in a very slow fashion and it can be calibrated by 'Bracketing' method (§5). Let ϕ_k^R designate the phase angle for red laser at which we measure the fourier phase φ_k in kth scanning, we have to verify that the phase angle for red laser in $k+1$th scanning ϕ_{k+1}^R equals to ϕ_k^R when measuring the fourier phase φ_{k+1}. However, 2π ambiguity exists between ϕ_k^R and ϕ_{k+1}^R, which will be removed by comparing $d\varphi/d\nu$.

The left panel of Fig. 6 shows the fourier phase at different wavelength channels as a function room temperature. The 8 wavelength channels are centered at 0.87, 0.92, 0.98, 1.04, 1.11, 1.20, 1.29, 1.41 and 1.55 μm respectively, which covers the working wavelength range of IR-ET. Change of fourier phase can be translated into RV drift via the equation:

$$\Delta v = \frac{\Delta\varphi}{2\pi}\frac{c\tau_0}{\lambda}, \tag{31}$$

the right panel of Fig. 6 shows the correlation between RV drift and room temperature. The RV drift is about 3500 $m/s/°C$, which put a tight constraint of temperature control. The precision of temperature control has to be 1 mK if we demand that the overall RV drift be limited within 3.5 m/s. We note that the thermal response we measured here refers to the entire optical system including the IR interferometer and the scanning interferometer.

5. THERMAL INSTABILITY CALIBRATION

In order to achieve high RV precision, system thermal instability has to be calibrated. We adopt 'Bracketing' method in observation, in which we take spectra of wavelength calibration sources before and after observation of science target. The exposure time for calibration source is approximately 2 minutes and 30 minutes for science target generally. We use φ_k to simulate 'Bracketing' method. We verify that the dispersion of φ_k for each wavelength channel is largely due to S/N. In fourier theory, 'Bracketing' method removes high frequency signal
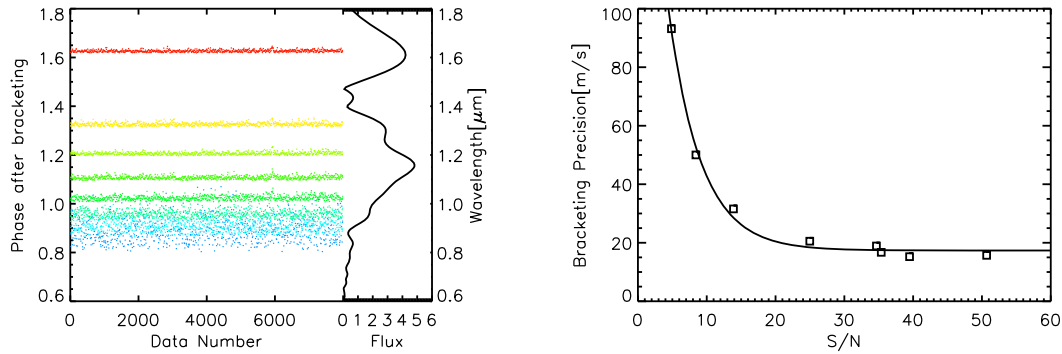
Figure 7. The left panel shows offset fourier phase after applying 'Bracketing' method, different colors represent different wavelength channels whose vertical positions correspond central wavelength. The spectrum is plotted along side. It is suggestive that there is correlation between dispersion of fourier phase and S/N of spectrum. The right panel shows the correlation between RV calibration precision and S/N. Solid line is the fitting based on the data in experiment.

because it is smoothed during the exposure of wavelength calibration source. In addition, it also removes the low frequency signal because the wavelength calibration exposures are used to track slow instrument drift (i.e. interferometer, spectrograph, CCD instability etc.). We use a fourier filter to filter out frequencies that are higher than 4.17 mHz (corresponding to half of frequency of 2 minutes exposures) and frequencies that are lower than 0.278 mHz (corresponding to half of frequency of 30 minutes exposures). The fourier phase series after fourier filtering are noises cannot be calibrated by 'Bracketing' method (Fig. 7).

$$\Delta v = \frac{\Delta \varphi}{2\pi} \frac{\tau_0}{\lambda} \cdot c, \tag{32}$$

It is suggested that the precision of 'Bracketing' calibration is dependent of S/N. We calculate the RV calibration precision of each wavelength channel. The correlation between RV calibration precision for single wavelength channel and S/N is given on right panel of Fig. 7. We use a exponential function to fit the relation between S/N and RV calibration precision and find that it can be approximated as:

$$\delta v = 17.35 + 209.6 \times \exp(-\frac{S/N}{4.74}), \tag{33}$$

In real observation, we have many wavelength channels (absorption or emission lines from calibration source spectrum) to monitor the instruments instability and the S/N is normally higher than that in our experiment. 100 channels with S/N of 50 translate into 1.74 m/s RV calibration precision due to 'Bracketing' method. We note that the RV calibration precision will be improved if the instrument is under temperature control since the influence of frequency range where the noise cannot be calibrated reduces as temperature fluctuation range decreases.

6. DISCUSSION AND CONCLUSION

We have introduced the design, fabrication and testing processes of a newly-built IR interferometer for IR-ET. We particularly present a new methodology of computing the fundamental limit of radial velocity (RV) measurement given by photon noise for DFDI (Dispersed Fixed Delay Interferometer) method as opposed to conventional echelle method. The new method is later used to determine the optical path difference (OPD) of the IR-ET interferometer. In addition, the new method can readily to calculate the fundamental RV uncertainty for a stellar spectrum of given effective temperature and $V \sin i$ at given spectral resolution. The new methodology can be widely used in simulation for RV measuring instruments adopting DFDI method.

We designed a experiment to measure the thermal response of the optical system including the IR interferometer and the scanning interferometer, which is 3500 $m/s/^\circ C$. The experiment uses a Fourier Transform

Spectrograph and a frequency-stabilized He-Ne laser ($\lambda_0 = 0.6328 \mu m$) to replace a conventional method of measuring optical system stability at single laser frequency. Further experiment to disentangle the thermal response of IR interferometer and that of scanning interferometer is necessary to investigate the contribution of thermal response from each component. The experiment can also be applied to thermal-optic effect measurement if temperature control system is incorporated.

We used the results from the thermal instability monitoring experiment to investigate the RV calibration precision of 'Bracketing' method, in which we take exposures of wavelength calibration source before and after observation of science target. We found that the RV precision of 'Bracketing' method is 1.74 m/s if there are 100 wavelength calibration channels with S/N of 50 available in calibration sources over the working wavelength region from 0.8 to 1.35 μm.

7. ACKNOWLEDGMENT

REFERENCES

[1] Bouchy, F., Mayor, M., Lovis, C., Udry, S., Benz, W., Bertaux, J., Delfosse, X., Mordasini, C., Pepe, F., Queloz, D., and Segransan, D., "The HARPS search for southern extra-solar planets. XVII. Super-Earth and Neptune-mass planets in multiple planet systems HD 47 186 and HD 181 433," *ApJ* **496**, 527–531 (Mar. 2009).

[2] Butler, R. P., Marcy, G. W., Williams, E., McCarthy, C., Dosanjh, P., and Vogt, S. S., "Attaining Doppler Precision of 3 M s-1," *PASP* **108**, 500 (June 1996).

[3] Bouchy, F., Pepe, F., and Queloz, D., "Fundamental photon noise limit to radial velocity measurements," *A&A* **374**, 733–739 (Aug. 2001).

[4] Ge, J., "Fixed delay interferometry for doppler extrasolar planet detection," *ApJ* **571**, 165–168 (June 2002).

[5] Erskine, D. J., "An externally dispersed interferometer prototype for sensitive radial velocimetry: Theory and demonstration on sunlight," *PASP* **115**, 255–269 (Feb. 2003).

[6] Wan, X., Ge, J., Wang, J., and Lee, B., "Monolithic interferometer for high precision radial velocity measurements," *Proc. SPIE* **7424**(1), 742406, SPIE (2009).

[7] Takaoka, E. and Kato, K., "Thermo-optic dispersion formula for aggas2," *Appl. Opt.* **38**(21), 4577–4580 (1999).

[8] Hossain, M. F., Chan, H. P., and Uddin, M. A., "Simultaneous measurement of thermo-optic and stress-optic coefficients of polymer thin films using prism coupler technique," *Appl. Opt.* **49**(3), 403–408 (2010).

[9] Hauschildt, P. H., Allard, F., and Baron, E., "The NextGen Model Atmosphere Grid for 3000¡T_eff¡10,000 K," *ApJ* **512**, 377–385 (Feb. 1999).

[10] Allard, F., Hauschildt, P. H., Alexander, D. R., Tamanai, A., and Schweitzer, A., "The Limiting Effects of Dust in Brown Dwarf Model Atmospheres," *ApJ* **556**, 357–372 (July 2001).

[11] Reiners, A., Bean, J. L., Huber, K. F., Dreizler, S., Seifahrt, A., and Czesla, S., "Detecting Planets Around Very Low Mass Stars with the Radial Velocity Method," *ApJ* **710**, 432–443 (Feb. 2010).

[12] Jenkins, J. S., Ramsey, L. W., Jones, H. R. A., Pavlenko, Y., Gallardo, J., Barnes, J. R., and Pinfield, D. J., "Rotational Velocities for M Dwarfs," *ApJ* **704**, 975–988 (Oct. 2009).

[13] Murphy, D. F. and Flavin, D. A., "Dispersion-insensitive measurement of thickness and group refractive index by low-coherence interferometry," *Appl. Opt.* **39**(25), 4607–4615 (2000).

[14] Rochford, K. B. and Dyer, S. D., "Demultiplexing of interferometrically interrogated fiber bragg grating sensors using hilbert transform processing," *J. Lightwave Technol.* **17**(5), 831 (1999).